


# Imaging plate scanners calibration and the attenuation behavior of imaging plate signals

Nan Bo(薄楠), and Nai-Yan Wang(王乃彦)

**Citation:**Chin. Phys. B, 2024, 33 (**6**): 060701. DOI: 10.1088/1674-1056/ad43d4
Journal homepage: http://cpb.iphy.ac.cn; http://iopscience.iop.org/cpb

**What follows is a list of articles you may be interested in**

---

## FPGA and computer-vision-based atom tracking technology for scanning probe microscopy

Feng-Du Yu(俞风度), Li Liu(刘利), Su-Ke Wang(王肃珂), Xin-Biao Zhang(张新彪), Le Lei(雷乐), Yuan-Zhi Huang(黄远志), Rui-Song Ma(马瑞松), and Qing Huan(郇庆)
Chin. Phys. B, 2024, 33 (**5**): 050705. DOI: 10.1088/1674-1056/ad34cb

## Calibration chain design based on integrating sphere transfer radiometer for SI-traceable on-orbit spectral radiometric calibration and its uncertainty analysis

Wei-Ning Zhao(赵维宁), Wei Fang(方伟), Li-Wei Sun(孙立微), Li-Hong Cui(崔立红), Yu-Peng Wang(王玉鹏)
Chin. Phys. B, 2016, 25 (**9**): 090701. DOI: 10.1088/1674-1056/25/9/090701

## Design and fabrication of structural color by local surface plasmonic meta-molecules

Ma Ya-Qi (马亚琪), Shao Jin-Hai (邵金海), Zhang Ya-Feng (张亚峰), Lu Bing-Rui (陆冰睿), Zhang Si-Chao (张思超), Sun Yan (孙艳), Qu Xin-Ping (屈新萍), Chen Yi-Fang (陈宜方)
Chin. Phys. B, 2015, 24 (**8**): 080702. DOI: 10.1088/1674-1056/24/8/080702

## Increasing rewriting speed of optical rewritable e-paper by selecting proper liquid crystals

Geng Yu (耿煜), Sun Jiatong (孙嘉瞳), Anatoli Murauski, Vladimir Chigrinov, Kwok Hoi Sing (郭海成 )
Chin. Phys. B, 2012, 21 (**8**): 080701. DOI: 10.1088/1674-1056/21/8/080701

---

**INSTRUMENTATION AND MEASUREMENT**

# Imaging plate scanners calibration and the attenuation behavior of imaging plate signals

Nan Bo(薄楠)[1,2] and Nai-Yan Wang(王乃彦)[2,†]

[1] *College of Nuclear Science and Technology, Beijing Normal University, Beijing* 100875, *China*
[2] *China Institute of Atomic Energy, Beijing* 102413, *China*

(Received 24 April 2024; accepted manuscript online 26 April 2024)

Based on previously reported work, we propose a new method for calibrating image plate (IP) scanners, offering greater flexibility and convenience, which can be extended to the calibration tasks of various scanner models. This method was applied to calibrate the sensitivity of a GE Typhoon FLA 7000 scanner. Additionally, we performed a calibration of the spontaneous signal attenuation behavior for BAS-MS, BAS-SR, and BAS-TR type IPs under the 20±1 °C environmental conditions, and observed significant signal carrier diffusion behavior in BAS-MS IP. The calibration results lay a foundation for further research on the interaction between ultra-short, ultra-intense lasers and matter.

**Keywords:** image plate, scanner, ultra-short ultra-intense lasers

**PACS:** 07.07.Hj, 07.60.Dq, 06.20.–f, 06.60.Jn **DOI:** 10.1088/1674-1056/ad43d4

## 1. Introduction

The interaction between ultra-short, ultra-intense lasers and matter is one of the most important frontier topics today.[1] It is widely believed that such interactions can produce unprecedented experimental phenomena or offer unprecedented experimental conditions.[2] With the development of laser technology, ultra-short, ultra-intense lasers have sparked infinite imagination and possibilities. Currently, research topics related to this are among the hottest worldwide.[3–7] This work discusses the diagnostic process of plasma generated by the interaction of ultra-short, ultra-intense lasers with solid targets, focusing on the calibration issues of image plate (IP) required in this diagnostic process.

Due to the temporal characteristics of ultra-short, ultraintense lasers, traditional electronics diagnostic methods may suffer from timely signal processing or congestion issues. Therefore, more "rudimentary" diagnostic methods have been adopted, despite their larger errors compared to traditional electronics diagnostics. Nowadays, passive, accumulative, and offline methods[8] are commonly used worldwide to diagnose plasma components at time scales of femtoseconds (fs) and picoseconds (ps), among which optical diagnostic methods[9] are also prevalent. Among these, a phosphorescent material known as an IP has been widely used.[10]

IP, as a type of phosphorescent emission medium with storage properties, is extensively applied in various scientific research and industrial practices, including biomedical and laser plasma studies, especially suitable for various radiation imaging-related issues. As shown in Fig. 1, IP has a layered structure, with the most significant layer being a barium fluoride phosphor doped with europium,[10,11] whose chemical formula is $BaFBr_xI_{1-x}:Eu^{2+}$. The first layer of the surface plays the role of protecting the phosphor layer, followed by the phosphor layer, and then the back layer and the substrate of the phosphor layer, followed by the ferromagnetic layer, which provides a certain magnetic attraction for the IP so that the IP can be fixed on the scanning plate when scanning or reading, and the last layer is to provide some protection for the magnetic layer. In different types of IPs, the specific thickness of each layer is different, especially the phosphor layer (such as, crystal particle size, density, etc. are different). When exposed to an ionizing radiation field, the phosphor layer can absorb and store a certain amount of energy, which ionizes $Eu^{2+}$ to $Eu^{3+}$, and the escaped electrons are trapped near the FBr in the form of $FBr^-$. The result is the formation of $Eu^{3+}$ ions and $FBr^-$ ions, where the spatial position of $Eu^{3+}$ ions is called the luminescence center, or lumen center, and the $FBr^-$ spatial position is called the color center or the F center. Because the F center is a crystal defect, it will absorb light of a specific wavelength and discolor the position. Subsequently, exposure to light of a specific wavelength, such as 650 nm, can induce the electrons to return to free state again and then transport them inside the crystal, recombining them into $Eu^{2+}$ when they hit $Eu^{3+}$ and releasing excess energy in the form of visible light photons, which is called photostimulated luminescence (PSL).[10,11] The working principle of IP is shown in Fig. 2. The released PSL is then collected by other photosensitive components (e.g., PMT) and converted into electrical signals, which are then digitized by an ADC and stored in a PC for further analysis. Due to its high sensitivity, wide dy-

†Corresponding author. E-mail: wangny@bnu.edu.cn

© 2024 Chinese Physical Society and IOP Publishing Ltd 

namic range, excellent spatial resolution, and critically, its immune to strong electromagnetic fields and reusable, IP is particularly suitable for detection in extreme environments like strong laser–matter interactions. Since IP does not inherently select energy, it is often used in conjunction with components that have energy-selective properties, forming part of an energy spectrum measurement system, such as electron magnetic spectrometers,[12] thomson spectrometers,[13] and stack spectrometers.[14] Therefore, studying the characteristics of IP is essential for conducting laser plasma experiments.

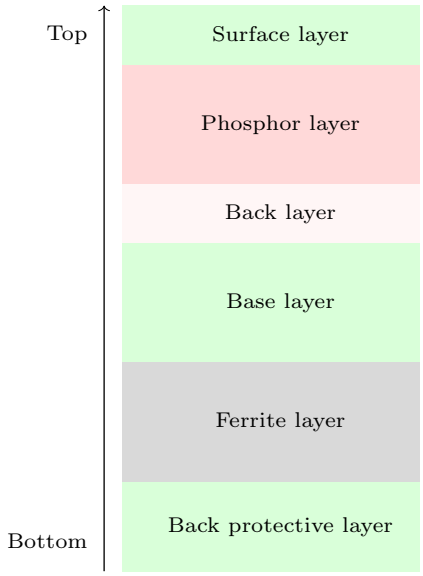



**Fig. 1.** Schematic diagram of IP structure.

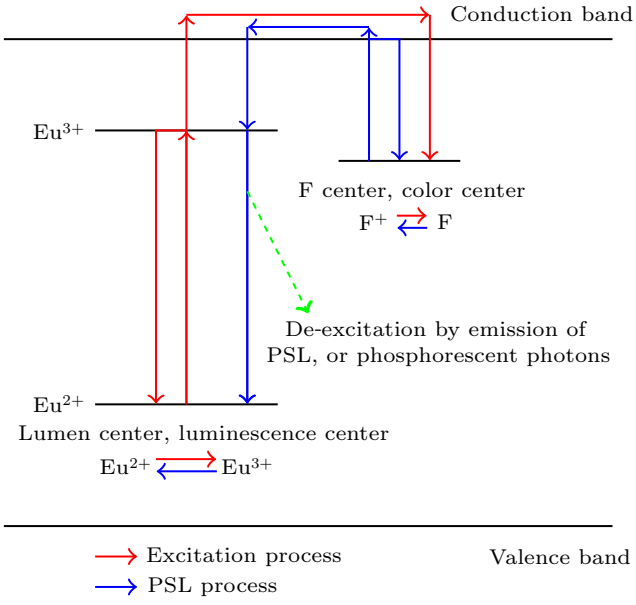



**Fig. 2.** IP energy level diagram and work.

This paper is structured into four main sections. Section 2 discusses the calibration of the sensitivity function of IP scanners; Section 3 identifies the spontaneous signal attenuation behavior of BAS-MS, BAS-SR, and BAS-TR type IP; Section 4 describes the data processing procedure; and Section 5 summarizes and discusses the work.

## 2. Scanner calibration

Prior to conducting quantitative analyses with IP, it is essential to calibrate the IP reader to ascertain the scanner's sensitivity function. Building upon existing research, we have optimized the calibration method to make it more flexible and rapid, applicable across various scanner models. This approach was applied successfully to a GE Typhoon FLA 7000 scanner in our laboratory.

For the GE scanning system, a specific relationship exists between photostimulable luminescence (PSL) and the grayscale values in the imagery, which can be mathematically expressed as follows:

$$\mathrm{PSL} = \left(\frac{G}{2^{16}-1}\right)^2 \left(\frac{R_{\mu\mathrm{m}}}{100}\right)^2 \times h(V)\, 10^{L/2}, \tag{1}$$

where $G$ represents the grayscale value obtained from a 16-bit square root encoded gel format image, $R_{\mu\mathrm{m}}$ indicates the pixel size during scanning, $h(V)$ denotes the scanner's sensitivity function (mainly related to the internal PMT voltage configuration), and $L$ stands for the dynamic range (which can be either 4 or 5). It is understood that PSL is directly determined by the energy deposited within the IP phosphor layer, and proportional to the total energy deposited,[15] which in turn is determined by the exposure conditions encompassing aspects such as the radiation source, IP type, exposure duration, and additional factors like ambient temperature, humidity, and ambient light. The image's grayscale value, $G$, correlates not only with the released PSL amount but also with the scanner gain $h(V)$, dynamic range $L$, and scanning pixel size $R_{\mu\mathrm{m}}$ during reading. The sensitivity $h(V)$ is an empirical relationship and highly individualized, varying significantly across different scanners. Determining the scanner's sensitivity function is a critical prerequisite for quantitative data analysis and cross-verification of data under varying environmental conditions, laying the groundwork for further laser–plasma interaction experiments. This calibration process aims to identify a concrete function for $h(V)$.

To determine the $h(V)$, we employ a simpler, flexible, and easily operable method, which requires just a radiation source and a single MS-type IP, eliminating the need for a previously calibrated scanner or known activity of the source. Firstly, by ensuring consistent exposure conditions, each exposure produces a constant PSL in IP, making it possible to generate a series of ($V$, $G$) pairs with fixed $R_{\mu\mathrm{m}}$ and $L$ settings along with changeable PMT voltage $V$ when scanning the IP. Then plot these data set on a $G$–$V$ figure and get the $G$–$V$ curve. We will obtain a function of $G$ with respect to

$V$ represented by $G = f(V)$ under a specific $R_{\mu m}$ and $L$ settings. Secondly, using a known exposure condition of a $^{14}C$ source with a total activity of 60 μCi and a diameter of 1 cm directly in contact with a MS-type IP for 20 min, followed by a 5 min rest in a controlled light-tight environment, results in 100 PSL/mm$^2$,[16,17] or 0.25 PSL/pixel when normalized to a 50 μm×50 μm area. This known condition allows for the calculation of a specific $G_0$ value when taken PSL = 0.25, $R_{\mu m} = 50$ μm and $L = 5$ into account along with $h(V_0)$ being any value in the field of positive real numbers, such as $h(V_0) = 0.1, 1, 4$. Please note that the $L$ should be consist with the setting deriving the $G$–$V$ curve as above. Thirdly, then inspect the $G$–$V$ curve, and find the point that the $G$ component is equal to $G_0$, so the corresponding $V = f^{-1}(G_0)$ component is our goal, in which $h(V) = h(V_0) = 0.1$, 1, 4 based on the above assumption. So, we identify three points in the sensitivity function, i.e., $(V, h(V))$ corresponds to $(x, y)$ in the coordinate system. Please note that we only used the value of $h(V_0)$, we don't know exactly what $V_0$ is, and we don't care about it. Subsequent adjustments to the $h(V_0)$ value and re-calculations using the $G$–$V$ curve enable the determination of the scanner's sensitivity function $h(V)$ under specific setting conditions, that is, $L = 5$ and $R_{\mu m} = 50$ μm. Change the settings of dynamic range $L$ and scan pixel $R_{\mu m}$, find the corresponding $G$–$V$ curve again, and repeat the above process to get the sensitivity curve under the corresponding settings.

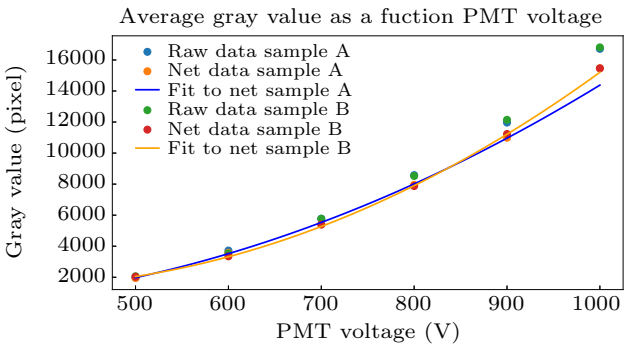



**Fig. 3.** The $G$–$V$ curve under $L = 5$ and $R_{\mu m} = 50$ μm.

This methodology was applied using a $^{90}Sr/^{90}Y$ beta source to calibrate the sensitivity of the GE Typhoon FLA 7000 scanner. The entire experiment was conducted under controlled conditions at 20±1 °C, and during nighttime to ensure darkness. With the source's activity around 2000 Bq and a diameter of 1 cm, the MS-type IP was exposed for 3 min and then scanned after a 270 min rest. This process produced a $G$–$V$ curve shown in Fig. 3 for $L = 5$ and $R_{\mu m} = 50$ μm. In order to ensure the repeatability of the data, the same test was done at two different time points, so there are two sets of data in Fig. 3. As can be seen from the figure, the results of the two independent experiments agree very well. The figure shows the experimental data before and after background correction, but because the background is very small, some points overlap with each other and cannot be seen visually. The data processing method and background deduction process will be discussed in Section 4. Figure 3 shows that the gray value $G$ of the image has a quadratic power relationship with the PMT voltage $V$. Using the expression

$$G = aV^2 + bV + c \tag{2}$$

to fit the data points, the fitting results are shown in Table 1.

**Table 1.** Curve fitting results under room temperature of 20 ± 1 °C, scanner dynamic range $L = 5$, and pixel size $R_{\mu m} = 50$ μm conditions.

| Sample point | $a$ | $b$ | $c$ |
|---|---|---|---|
| Sample A | 0.02 | –10.32 | 1281.65 |
| Sample B | 0.03 | –24.66 | 5880.38 |

After obtaining $G = f(V)$ curve, $h(V_0)$ is continuously valued from 0.1 and 4.0 in steps of 0.1 and substituted into

$$\mathrm{PSL}_{50\ \mu m} = 0.25 = \left(\frac{G}{2^{16}-1}\right)^2 \left(\frac{R_{\mu m}}{100}\right)^2 \times h(V_0)\, 10^{5/2} \tag{3}$$

to obtain a series of gray value $G_0$. Then reuse these $G_0$ values inversely to solve function $G = f(V)$, eventually get $V = f^{-1}(G_0)$. The sensitivity curve of GE Typhoon FLA 7000 scanner $h(V)$ can be obtained by drawing the voltage value and the corresponding $h(V)$ value in the coordinate system. The results are shown in Fig. 4. This curve is the sensitivity curve under the conditions of $L = 5$ and $R_{\mu m} = 50$ μm. The sensitivity function of the scanner under other conditions can be obtained by modifying the settings. It can be determined from Fig. 4 that when the PMT voltage is 800V, $h(V)$ is equal to 0.16, which still has a certain gap with the reference value 0.1, which once again emphasizes the importance of targeted calibration of specific scanners. This result will serve the quantitative analysis process of laser plasma diagnosis.

It is crucial to underline that the given value of 100 PSL/mm$^2$ is based on experiments using the BAS-MS type image plate. Consequently, the grayscale value $G_0$ derived from this data is inherently linked to the characteristics of the MS type, and any $G$–$V$ curve used for reference must also originate from a BAS-MS type IP. This stipulation necessitates the use of BAS-MS type IP when employing this method for scanner calibration. The derived sensitivity curve $h(V)$ of the scanner system is an intrinsic attribute of the system itself and is not limited by the type of the IP.

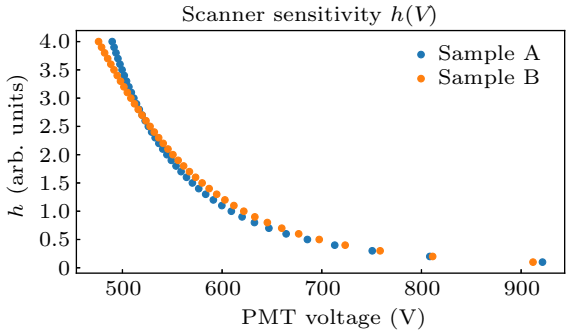



**Fig. 4.** Sensitivity curve of GE Typhoon FLA 7000 scanner.

## 3. IP signal attenuation

Ionizing radiation deposits energy in image plates by exciting phosphorescent materials to higher energy states, which is temporarily stored. This state is unstable. Aside from active human intervention to return it to the ground state, external disturbances and the system's spontaneous drive towards the lowest energy "stable state" reduce the higher energy components. Therefore, under constant external conditions, electrons temporarily bound around F($Br^-$) spontaneously return to $Eu^{3+}$, causing the signal stored in the IP to exhibit spontaneous attenuation over time. Quantitative analysis of laser plasma experiment results requires knowledge of the signal quantity in the IP at the end of irradiation, while the data read from scanning the IP only represents the signal quantity that has not yet been lost at the moment of scanning. Thus, the law of IP signal attenuation plays a role in correcting the observed results to obtain the true experimental data. It is necessary to determine the spontaneous attenuation law of the IP signal over time. For this purpose, based on the external environment at the time of this work, a quantitative analysis of the spontaneous attenuation behavior of the IP signal was conducted.

The spontaneous decay law of the IP signal over time is denoted as $f(t)$, representing the percentage of the signal in the IP at moment $t$ that has not yet been lost compared to the signal at $t=0$, or the probability that the signal has not yet been lost at moment $t$. Since signal loss also occurs during the irradiation process, the accumulated signal quantity in the IP at the end of irradiation is the convolution of the radiation source's impact response function $R(t)$ with the signal spontaneous fading function $f(t)$

$$S(\tau)=\int_0^{\tau} R(t)\,f(\tau-t)\,\mathrm{d}t, \tag{4}$$

where $\tau$ is the duration of irradiation, and $R(t)$ should be a step function with changing amplitude because of the nature of IP. If the time interval from the end of irradiation to scanning the IP is $T$, then the remaining signal quantity at moment $\tau+T$ is

$$S(\tau,T)=\int_0^{\tau} R(t)\,f(\tau+T-t)\,\mathrm{d}t. \tag{5}$$

For ease of timing and subsequent data processing, the timing starting point is reselected, choosing the moment when the irradiation of the IP is completed as the starting point, then the formula further becomes

$$S(\tau,T)=\int_{-\tau}^{0} R(t)\,f(T-t)\,\mathrm{d}t. \tag{6}$$

The schematic process of signal quantity evolution over time is shown in Fig. 5.

For a stable radiation source, its impact response function $R(t)$ is constant $R$ and does not change over time, which can be taken outside the integral sign. If for a fixed scanning time $T$ (i.e., its differential $\mathrm{d}T=0$), then

$$\lim_{\tau\to 0}\frac{S(\tau,T)}{\tau R_0}=f(T). \tag{7}$$

Therefore, to obtain $f(t)$ from the above relationship, the irradiation duration must tend to 0, requiring a very strong radiation source for impact response testing of the IP. However, this is only possible in ultra-short, ultra-intense laser experiment. For approximation, when $T\gg\tau$, it can be assumed that the condition $\tau\to 0$ is satisfied, and then the signal attenuation behavior after a longer waiting time can be approximated as the "true" signal attenuation function $f(t)$.

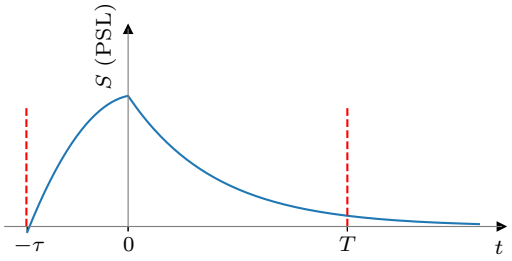



**Fig. 5.** Schematic diagram of IP signal evolution over time.

We tested the signal attenuation function $f(t)$ of three types of IP, BAS-MS, BAS-SR, and BAS-TR, using the same $^{90}Sr/^{90}Y$ electron source, with room temperature controlled at 20±1 °C, and the electron source directly in contact with the IP, as shown in Fig. 6, irradiating for 1 min to reduce signal fading during the irradiation process. Although the closer to the end of irradiation, the greater the error in the scanning results, which cannot well represent the "true" signal attenuation behavior, we still statistically analyzed the signal attenuation behavior of the IP from 2 min after the end of irradiation to up to 840 min, and repeated measurements were made for some data points, with the results at $t=2$ min used as the standard for normalization. The results for the three types of IPs are shown in Fig. 7. The results of other work are also shown. The figure shows the data before and after background correction. The blue dot in the figure is the average gray value of the image obtained by direct scanning, which is the raw data, while the orange dot is the data after background correction, which is the net data.

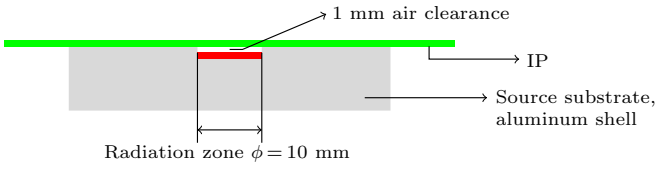



**Fig. 6.** Schematic diagram of IP irradiated by radioactive sources.

According to previous works, a general consensus is that the spontaneous attenuation behavior of IP signals follows an exponential distribution. However, due to differences in the time regions of interest to different authors and the different

external environments, some authors observed attenuation behavior following a single exponential distribution,[18] while others observed a double-exponential distribution.[15,17,19] In this work, using a double-exponential function

$$f(t) = A_1 \cdot \mathrm{e}^{-\frac{t}{\tau_1}} + A_2 \cdot \mathrm{e}^{-\frac{t}{\tau_2}} \tag{8}$$

fits to the background corrected data (i.e., net data) better than a single exponential. Here, $t$ is the time elapsed after the end of the exposure and $A_i$, $\tau_i$ are the amplitude and time constants, respectively. Fits of data using Eq. (8) are also shown in Fig. 7 and the fitting parameters are summarized in Table 2.

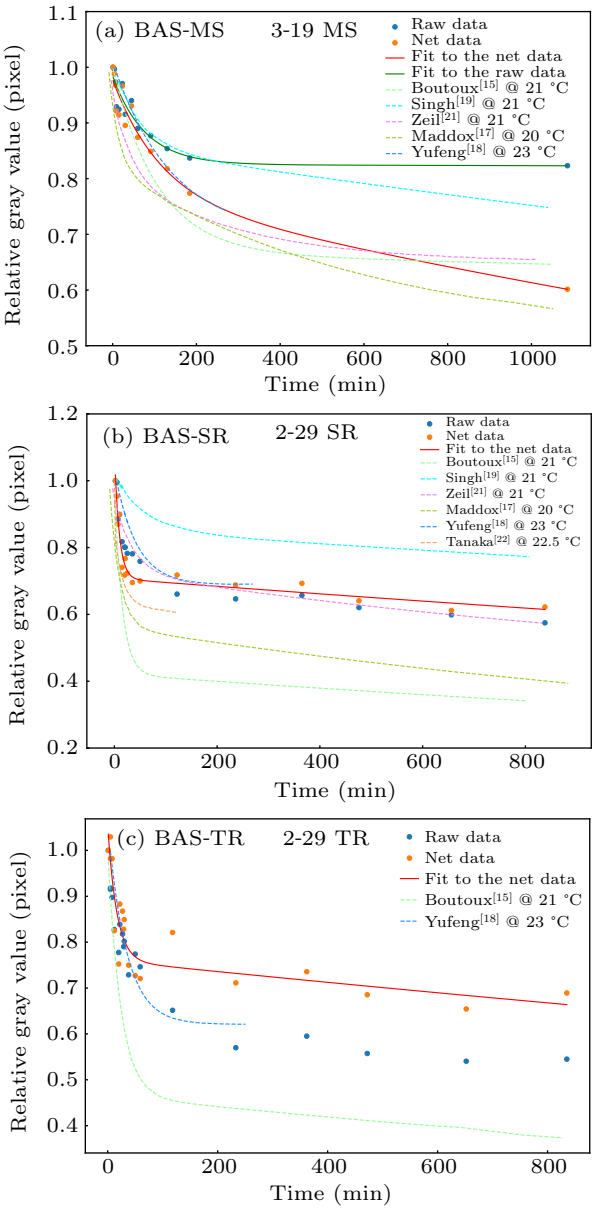



**Fig. 7.** IP signal fading process from the end of irradiation 2 min to 840 min at the ambient temperature 20±1 °C.

From Fig. 7, it is evident that BAS-SR and BAS-TR decay faster than BAS-MS, which is consistent with the previously reported works qualitatively. Seriously speaking, for an E-exponential decay process, the characteristic time (i.e., half-time) of the decay is $T_{1/2} = \tau_i \times \ln 2$. To be safe, it is okay to just think about $\tau_i$, because $\tau_i \times \ln 2 < \tau_i$. As a result, the fast component of BAS-SR is roughly about 10 min, the slow component is about 6000 min. The proportion of fast to slow components is about 3:7. Because the fast component dominates the initial stage of signal attenuation, if data collection is carried out at this time, the uncertainty of the result will increase. Considering that the characteristic time of the fast process is about 10 min, data collection should be carried out at least 5 times the time scale to ensure that the data acquisition is in the stage that the signal attenuation behavior becomes relatively stable. However, the time span should not be pulled too long, because the longer the time, the signal-to-noise ratio in the IP may get worse, according to the exponential distribution law, the choice of 5 to 7 times the time scale is more appropriate. On the whole, for BAS-SR type IP in laser plasma diagnostic experiment, it is recommended to collect data at about 60 min after laser shooting stops.

**Table 2.** Fitting parameters for the fading of three kinds of IPs under 20±1 °C temperature conditions.

| Data & IP type | $A_1$ | $\tau_1$ (min) | $A_2$ | $\tau_2$ (min) |
|---|---|---|---|---|
| 3-19 MS | 0.21 | 112.4 | 0.77 | 4380.7 |
| 3-19 MS (raw data) | 0.16 | 77.2 | 0.83 | 431574.7 |
| 2-29 SR | 0.38 | 9.4 | 0.71 | 5990.7 |
| 2-29 TR | 0.29 | 16.5 | 0.76 | 6174.4 |

For the BAS-TR type IP, because its phosphor layer is the thinnest among the three and there is no protective layer on the front surface, the BAS-TR type IP suitable for the detection of heavy charged particles, and the image quality from the scan should be better, but the detection efficiency of high-energy ionizing radiation may also be the lowest. As shown in Fig. 7(c), the fast decay process of the BAS-TR IP is about 15 min, which is slightly longer than that of the BAS-SR type 10 min, but the slow decay process is basically the same, which is about 6000 min. In the laser plasma diagnostic experiment, for BAS-TR type IP, it is recommended to read at about 90 min after laser stops.

Figure 7(a) shows the signal attenuation behavior of the BAS-MS type IP. The orange line is the fitting of net data after background correction, while the green line is the fitting of the raw data before background correction. The orange line indicates that the fast component is 112.4 min and the slow component is 4380.7 min, indicating that the fast decay of the MS-type IP is much slower than that of BAS-SR and BAS-TR. Furthermore, the attenuation process of BAS-MS shows a different phenomenon from that of BAS-SR and BAS-TR: the evolution of the raw signal and the net signal over time is inconsistent. The green and orange lines showed an increasingly distinct gap over time, which was not observed in the BAS-SR and BAS-TR results. It can be observed from Figs. 7(b) and 7(c) that the raw signal and the corresponding net signal have the same evolutionary behavior over time, fade at the same

rate, or fluctuate up and down, but the fluctuation process is also consistent. However, in the BAS-MS type IP, the raw signal does not decrease significantly during the period from 200 min to 1100 min, while the net signal after subtracting the background shows an obvious attenuation. This shows that during the period from 200 min to 1100 min, the background signal gets stronger, which is a very puzzling phenomenon. The MS-type IP was kept at constant temperature and humidity and under dark light conditions, why did the background signal not decline over time, but increased? The difference between the green line and the orange line in Fig. 7(a) represents the background signal. It can be clearly observed that the background signal increases continuously not only during the process from 200 min to 1100 min, but also from the time zero. Therefore, after careful consideration, the author ruled out the possibility of introducing external radiation sources in the process of preserving MS-type IP, and suspects that one possible reason for this phenomenon is that the spontaneous diffusion process of message carriers on the BAS-MS IP is faster and more obvious. Similar concerns have been raised in the work of Andrew Harrison.[20]

## 4. Data processing

In this study, the $G$ values used were derived from data that underwent background correction. The imaging plates used for each type came from the same production batch. A single IP was cut sufficiently large so that areas outside the electron source exposure region were considered as the background area. Four circular areas were randomly selected around the perimeter of the exposure area, and their average grayscale value was calculated as the background signal and subtracted from the exposure area. The three-dimensional distribution of the signal scanned from a BAS-MS IP is illustrated in Fig. 8. To determine the exposure area of the electron source, the raw image is copied and this gel format images were first processed with a Gaussian filter to smooth pixel values and eliminate spike noise. Subsequently, a statistical histogram of pixel values across the entire image was generated, expectedly revealing two distinct peaks. A histogram corresponding to Fig. 8 is shown in Fig. 9. The lowest position between the two peak positions was then calculated to serve as the lower threshold limit. After setting the threshold, the remaining area in the copied image was designated as the effective exposure area, or region of interest (ROI). This ROI region is ported to the raw image to determine the signal analysis area. Four circular areas were then randomly selected in distant regions surrounding the signal, and their average value was taken as the background level. As shown in Fig. 10, label 1 represents the signal region, and labels 2 to 5 represent background zones. The data for these five regions are summarized in Table 3.

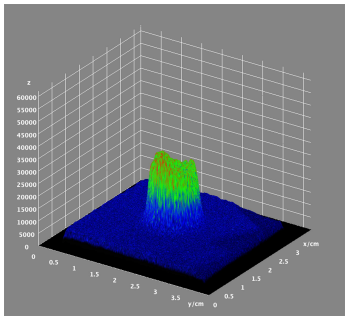


**Fig. 8.** A typical BAS-MS IP signal. Colors are added manually for clarity.

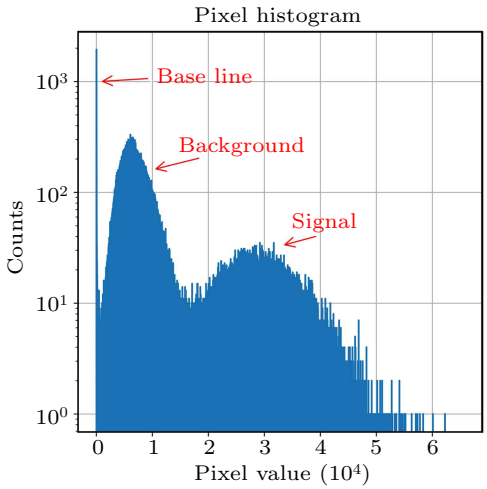



**Fig. 9.** A histogram of the typical distribution about MS IP. The peak on the far right is from the signal, and the background signal is on the left.

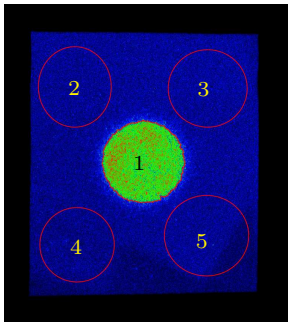



**Fig. 10.** Signal and background zones. Label 1 is the signal, and 2 to 5 are considered as the background representation.

**Table 3.** The data corresponding to Fig. 10.

| Label | Area ($cm^2$) | Mean | StdDev | Mode | Median | Min | Max |
|---|---|---|---|---|---|---|---|
| 1 | 0.9 | 28407.5 | 6515.8 | 29210 | 28070 | 8184 | 62258 |
| 2 | 0.8 | 6589.7 | 2172.3 | 6078 | 6404 | 740 | 20921 |
| 3 | 0.8 | 6928.7 | 2213.8 | 6037 | 6763 | 1013 | 23388 |
| 4 | 0.8 | 6001.9 | 2051.3 | 5627 | 5822 | 651 | 19115 |
| 5 | 0.9 | 6275.3 | 2175.8 | 6400 | 6085 | 386 | 23003 |

## 5. Conclusion

In this study, we discussed a new method for calibrating the sensitivity curve of imaging plate scanners. This method is simpler, more flexible, and easier to operate, making it applicable for the calibration tasks of scanners across all models. Utilizing this approach, we successfully calibrated a GE Typhoon FLA 7000 scanner. The calibration results indicated

that at a PMT voltage of 800 V, the scanning system's gain was $h(V) = 0.16$. Furthermore, within the laboratory's ambient temperature of $20 \pm 1$ °C, we characterized the spontaneous attenuation behavior of signals from three types of IPs over time. Our results revealed that the signal attenuation of the three types of IPs involves two processes: a rapid attenuation phase followed by a slower one. Among these, the BAS-SR and BAS-TR generally exhibited faster signal attenuation compared to BAS-MS, aligning with some previous studies. But, in the BAS-MS IP, the carrier diffusion phenomenon was more obvious than the rest two.

To minimize errors caused by signal attenuation during the reading process, the author recommends collecting IP signals during the slow component phase after irradiation in laser plasma diagnostic experiments. For SR-type IP, 60 minutes after the laser stops shooting is recommended; for TR-type is 90 minutes; and for MS-type, because the signal decay takes the longest time to reach the slow component phase, the recommended scanning time is 500 to 700 minutes, which is much longer than the 60 min and 90 min required for SR and TR. In addition, it is considered that the carrier diffusion of the MS-type IP is more obvious, its signal-to-noise ratio may not be better than the other two. Therefore, for the thermal electron diagnostic experiment in laser plasma, the author recommends the use of SR-type IP, because it has a thicker sensitive layer than TR, the detection efficiency of ultra-hot electrons will be higher, and the spatial resolution will be better, and the SR-type has a protective layer that can provide protection for the phosphor layer under the ultrabright radiation source generated by laser plasma.

This study not only advances the understanding of IP signal behavior but also provides practical recommendations for improving the accuracy of collecting IP signal.

## Acknowledgements

This work was supported by the Nuclear Industry Academician Fund, the National Natural Science Foundation of China (Grant No. 1220051312), and Young Talents Fund of China National Nuclear Corporation (Grant No. FY212406000901). Special thanks are extended to Professors Zheng Yun and Li Tianxiao for providing the $^{90}$Sr/$^{90}$Y electron source. We are particularly grateful to Professor Wang Nian for providing the $^{14}$C electron source. Acknowledgements also go to Professors Wang Zhao, He Chuangye, Li Jing, and Wu Haicheng for their support in providing dark and constant temperature environments.

## References

[1] Salamin Y I, Hu S X, Hatsagortsyan K Z and Keitel C H 2006 *Phys. Rep.* **427** 41
[2] Günther M M, Rosmej O N, Tavana P, Gyrdymov M, Skobliakov A, Kantsyrev A, Zähter S, Borisenko N G, Pukhov A and Andreev N E 2022 *Nat. Commun.* **13** 170
[3] Rosmej O N, Andreev N E, Zaehter S, Zahn N, Christ P, Borm B, Radon T, Sokolov A, Pugachev L P, Khaghani D, Horst F, Borisenko N G, Sklizkov G and Pimenov V G 2019 *New J. Phys.* **21** 043044
[4] Rosmej O N, Suslov N, Martsovenko D, *et al.* 2015 *Plasma Phys. Control. Fusion* **57** 094001
[5] Arikawa Y, Kojima S, Morace A, *et al.* 2017 *Nucl. Fusion* **57** 066022
[6] Bin J H, Obst-Huebl L, Mao J H, *et al.* 2022 *Sci. Rep.* **12** 1484
[7] Ewald F, Schwoerer H, Düsterer S, Sauerbrey R, Magill J, Galy J, Schenkel R, Karsch S, Habs D and Witte K 2003 *Plasma Phys. Control. Fusion* **45** A83
[8] Hidding B, Pretzler G, Clever M, Brandl F, Zamponi F, Lübcke A, Kämpfer T, Uschmann I, Förster E, Schramm U, Sauerbrey R, Kroupp E, Veisz L, Schmid K, Benavides S and Karsch S 2007 *Rev. Sci. Instrum.* **78** 083301
[9] Batani D, Santos J, Forestier-Colleoni P, Mancelli D, Ehret M, Trela J, Morace A, Jakubowska K, Antonelli L, Sorbo D, Manclossi M and Veltcheva M 2019 *J. Fusion Energy* **38** 299
[10] Rowlands J A 2002 *Phys. Med. Biol.* **47** R123
[11] Bonnet T, Comet M, Denis-Petit D, Gobet F, Hannachi F, Tarisien M, Versteegen M and Aleonard M M 2013 *Rev. Sci. Instrum.* **84** 013508
[12] Glenn G, Tiwari G, Dyer G, Curry C, Donovan M, Gaul E, Gauthier M, Glenzer S, Gordon J, Hegelich B, Martinez M, McCary E, Spinks M and Ditmire T 2019 *J. Instrum.* **14** P03012
[13] Kojima S, Inoue S, Dinh T H, Hasegawa N, Mori M, Sakaki H, Yamamoto Y, Sasaki T, Shiokawa K, Kondo K, Yamanaka T, Hashida M, Sakabe S, Nishikino M and Kondo K 2020 *Rev. Sci. Instrum.* **91** 053305
[14] Behrens R and Ambrosi P 2002 *Radiat. Prot. Dosimetry* **101** 73
[15] Boutoux G, Rabhi N, Batani D, Binet A, Ducret J E, Jakubowska K, Nègre J P, Reverdin C and Thfoin I 2015 *Rev. Sci. Instrum.* **86** 113304
[16] Williams G J, Maddox B R, Chen H, Kojima S and Millecchia M 2014 *Rev. Sci. Instrum.* **85** 11
[17] Maddox B R, Park H S, Remington B A, Izumi N, Chen S, Chen C, Kimminau G, Ali Z, Haugh M J and Ma Q 2011 *Rev. Sci. Instrum.* **82** 023111
[18] Dong Y, Zhang Z, Xu M, Du Y, Zhang C, Dong X, He Y, Tan J, Zhang Y, Zhu C, Feng J, Cheng L, Li Y and Li Y 2020 *Rev. Sci. Instrum.* **91** 033105
[19] Singh S, Slavicek T, Hodak R, Versaci R, Pridal P and Kumar D 2017 *Rev. Sci. Instrum.* **88** 075105
[20] Harrison A, Lane L C, Templer R H and Seddon J M 1991 *Nucl. Instrum. Methods Phys. Res. A* **310** 220
[21] Zeil K, Kraft S D, Jochmann A, Kroll F, Jahr W, Schramm U, Karsch L, Pawelke J, Hidding B and Pretzler G 2010 *Rev. Sci. Instrum.* **81** 013307